Dynamic simulation of a novel nuclear hybrid energy system with large-scale hydrogen storage in an underground salt cavern

An Ho, Lars Capener

Nomenclature

Abbreviations

IGV	Inlet Guide Vane
LHV	Low Heating Value
LWR	Light Water Reactor
NHES	Nuclear Hybrid Energy System
PEM	Polymer Electrolyte Membrane
SMR	Small Modular Reactor

Symbols

n_{neu}	Neutron density
t	Time
ρ_{nuc}	Reactivity
β_{mix}	Effective delayed neutron fractions
Λ	Neutron generation time
λ	Decay constant for single group of delayed neutrons
C_{neu}	Concentration of single average group of delayed neutrons
T	Temperature
α	Temperature feedback coefficient
z	Control rods position
p_2, p_1, p_0	Control rods parameters
ρ	Density
V	Volume
C_p	Heat capacity
W	Power
h_{conv}	Convective heat transfer coefficient
A_s	Surface area
$\dot{m}$	Mass flow rate
E_f	Average recoverable energy per fission
σ_f^{235}	Microscopic cross section of Uranium 235
N_{235}	Atomic number density of Uranium 235
κ_m	Thermal conductivity of the coolant
Dh	Hydraulic diameter
Re	Reynolds number
Pr	Prandtl number
Nu	Nusselt number
$\dot{m}$	Mass flow rate
η	Efficiency
$\dot{N}$	Molar flow rate
I	Current
F	Faraday's constant
$\dot{n}$	Molar flow rate per area
y	Molar fraction
C	Concentration

P	Pressure
R	Gas constant
δ_e	Thickness
D_{eff}	Effective diffusion coefficient
n_d	Electro-osmotic drag coefficient
D_w	Diffusion coefficient of water
t_{me}	Membrane thickness
ϵ	Porosity of electrodes
ϵ_p	Percolation threshold
D_{A-B}	Binary diffusion coefficient for species A and B
T_c, P_c, MW	Critical temperature, pressure and molecular weight
Vol	Real cell voltage
E	Ideal open circuit voltage
η_{act}	Activation overvoltage
η_{ohm}	Ohmic overvoltage
E_{rev}^0	Reversible cell potential
i_0	Exchange current density
α_{an}	Charge transfer coefficients at anode
α_{cat}	Charge transfer coefficients at cathode
σ_{me}	Material conductivity
n_{H_2}	Number of hydrogen moles
h_{cav}	Convective heat transfer coefficient between the hydrogen gas inside the cavern and the wall of the cavern
z_{comp}	Hydrogen compressibility factor
H	Enthalpy
g	Gravitational acceleration
D	Cavern depth
H	Cavern height
i	Current density
λ	Membrane water content
PR_c	Compression ratio
γ_c	Cold end ratio of specific heat
θ_{IGV}	Angle of IGVs
T_{fire}	Turbine firing temperature
η_{comb}	Combustion efficiency
γ_h	Hot end ratio of the specific heats
Subscripts	
an	Anode
cat	Cathode
in	Inlet
out	Outlet
gen	Generated
mem	Membrane
$cons$	Consumed

eod	Electro-osmotic drag
$diff$	Diffusion
act	Activation
is	Isentropic
$turb$	Turbine
$therm$	Thermal
$core$	Nuclear reactor core
m	Coolant
H_2	Hydrogen
w	Wall
cav	Cavern
$comp$	Compressor
$steam$	Steam
$elec$	Electrolyzer
nom	nominal
a	Air
o	Reference
e	Exhaust
amb	Ambient
$GasTurb$	Gas turbine
$Brayton$	Brayton cycle
$recup$	Recuperator

1. Introduction

The electricity market in the United States is moving away from fossil fuel sources and towards a mixed energy source market, with emphasis on renewable energy such as solar, wind, etc. However, an increase in variable renewable energy sources in the grid system causes technical and economic challenges due to the high variability, intermittency and low-capacity factors of renewable energy plants [1], [2], [3]. Power systems with integrated renewable energy sources require greater system flexibility at all times to make sure the supply-demand balance is maintained [4], [5], [6]. To meet the demands that are not met by renewable energy sources, load following power plants are usually needed to replace the renewable sources during peak demands. Natural gas power plants are usually used for this purpose [7], which have low capital cost and high operating cost and emit significant greenhouse gases [8]. To be able to decarbonize and work towards a green and clean future of electricity, traditional and reliable sources must be replaced by other low or free carbon sources such as nuclear power plants [9], [10].

Nuclear power plants offer several benefits such as high reliability, high-capacity factors, and a low carbon footprint [11]. However, to maximize the benefit of nuclear power plants, they must be operated at maximum capacity at all times to minimize the LCOE for these plants. Further, accelerated fuel depletion can develop when nuclear power plants have to ramp up and down to meet the grid demand. Nuclear power plants often operate at “base load” during low demand time, and sell surplus electricity to the grid usually at low or negative prices [8], [12]. This is because

renewable energies peak at certain times of the day, which leads to volatile daily prices. During high renewable capacities, the market price of electricity can go down to negative values [13].

Nuclear power's problem of inflexibility is due to both technical and economic reasons. Nuclear reactors adjust power primarily by changing the control rods positions to moderate the power output. Changing the position of the control rods drastically changes the neutron flux profile surrounding the fuel assemblies, which in turn changes the heating rate around the control rods. This power change causes the fuel assembly temperature to undergo immediate and significant changes. Fuel pellets and cladding undergo serious thermal and mechanical stresses that can result in the fuel pellets cracking or the cladding failing [12], [14], [15]. Hence, the speed at which the control rods can be inserted or withdrawn is controlled by the Nuclear Regulatory Commission [12]. As a result, nuclear power can be difficult to integrate into an increasingly diverse electricity market, with more and more carbon-free renewable sources.

However, studies have shown that integrating nuclear power plants with other sources can increase the flexibility and reliability of the system, reduce the cost, maximize revenues, and help meet greenhouse gas reduction goals [12]. These integrated hybrid energy systems store and/or use the excess electricity/heat to produce different commodities [16], [17], [18]. This will allow the base load operation of nuclear power plants and other renewable sources to minimize cost, maximize profit and provide low-carbon electricity generation to the grid. An example of such a nuclear generated commodity is hydrogen.

Hydrogen is a promising fuel that is light, storable, and most importantly, does not produce any pollutants or greenhouse gases. It is the most energy dense of any known fuel material [19]. It is also a very valuable commodity, with its demand rising more than 300% since 1975, and it is expected to continue to rise in the next decades [20]. Hydrogen is used in different industries including oil refining, methanol production, ammonia synthesis, etc. It can also be used in transportation, building heating (especially for multifamily or commercial buildings), and power generation [21]. Hydrogen has been used for storing renewable energy, as well as in gas turbines to produce electricity. The International Energy Agency (2019) emphasized the potential of hydrogen to facilitate the transition into a cleaner, greener and more affordable energy future [21].

Salt caverns have been used to store various forms of energy including oil, natural gas, and hydrogen [22]. Salt cavern storage is considered among the most promising underground gas storage options due to the large sealing capacity of rock salt, the low cushion gas requirement, the inert nature of salt caverns, and the ability to operate flexibly with high injection/withdrawal rates [23]. Currently, there are a few sites that store hydrogen in salt caverns such as Teeside, United Kingdom, and Clemens Dome, Spindletop and Moss Bluff in the United States [24]. Clemens Dome salt cavern facility has been in operation since 1983, and has shown remarkable resiliency and reliability, demonstrating that underground salt cavern hydrogen storage is a technically feasible option. Salt caverns also offer an economic incentive, as it can be up to 10 times less expensive than above ground storage tanks, as well as 20 times less than hard rock mines [25].

Numerous studies have been presented in the literature regarding different nuclear hybrid energy systems. For example, Wang et al. [26] proposed a nuclear-solar hybrid system for

combined power and freshwater production. The authors proposed a novel design of a nuclear-solar hybrid power plant with heavy liquid metal as the heat transfer medium. A technical and economic analysis was performed to evaluate the performance of the hybrid model. The results showed that the proposed design was technically feasible, and had an annual cost saving of $680,423 compared with a desalination system powered by a coal-fired plant. Ingersoll et al. [27] proposed a desalination system powered by a small modular nuclear reactor. In the proposed hybrid system, the nuclear plant, a NuScale module, was combined with three different desalinations systems: multi-effect distillation, multi-stage flash distillation, and reverse osmosis. The results showed that the nuclear power plant could be effectively coupled with a water desalination plant. Epiney et al. [6] carried out an economic analysis of a hybrid nuclear system in a grid system with wind turbines. The authors used a new methodology to evaluate the economic performance of the hybrid system. The new methodology incorporates the stochastic characteristics of a nuclear-renewable hybrid energy system like wind speed or electricity demands. The results showed that under the right conditions, with suitable industrial processes being added, the hybrid system could provide economic benefits. Zhao et al. [28] proposed a novel design and performed a preliminary performance analysis on a hybrid nuclear-solar system using a molten-salt packed-bed thermal energy storage. The proposed system integrated a molten-salt concentrating solar power tower plant with small modular reactors. A thermal energy storage system was used to store and dispatch thermal energy whenever it is required. The proposed system was able to satisfy the power demand in a 7-day operation without the need for any heat generation restrictions. The results showed the technical feasibility of the hybrid system as well as the potential for a non-carbon emitting power generation system for load following applications.

A review of the literature also shows that there are a few studies on the dynamic modeling of hybrid nuclear hydrogen energy systems. Many reports and reviews have been presented about different technologies for hydrogen production with nuclear reactors [1], [29], [30]. Pinsky et al. [1] reviewed the current hydrogen generation technologies coupled with nuclear energy. It was shown that electrolysis and thermochemical water splitting technologies can easily be coupled with nuclear plants. El-Emam et al. [29] showed that with the current hydrogen generation technologies, nuclear energy is one of the main alternatives that can meet the required thermal/electrical needs for large-scale hydrogen production. Şahin et al. [30] specifically looked at coupling Gen IV nuclear reactors with hydrogen generation technologies. The authors discussed that nuclear energy can be used as the primary energy source for large-scale hydrogen production to achieve a sustainable energy future. Obrien et al. [31] carried out an analysis to evaluate large-scale hydrogen production using nuclear energy. However, in all of these studies, a steady-state analysis was conducted and flexible operation of nuclear power plants was not considered. Kim et al. [8] conducted a study on the dynamic performance of a high temperature steam electrolysis integrated with a nuclear hybrid energy system. However, the limitation of this study was that the dynamic simulation was limited to a 7-day period at the longest.

In this study, a novel nuclear-hydrogen hybrid system is proposed that integrates a small modular reactor (SMR) module with a steam Rankine cycle, a polymer electrolyte membrane

(PEM) electrolyzer, a large-scale hydrogen storage system with an underground salt cavern, and a hydrogen gas turbine cycle. The primary objective of the study is to demonstrate the technical feasibility as well as the benefits of the proposed system under a highly variable grid demand requiring flexible outputs. A dynamic model was developed for each subsystem of the proposed hybrid system to simulate its performance for a year-long period, using real data from the grid. A reliable control scheme was developed for the nuclear reactor and the hydrogen gas turbine. Using the developed dynamic model and control schemes, the technical feasibility of the proposed hybrid system is evaluated and then compared with a stand-alone nuclear power plant. The main novelty of this study is the proposal of a novel nuclear hybrid energy system and dynamic simulation of its performance for a period of one year.

The rest of the paper is organized as follows: Section 2 provides an overview of the nuclear hybrid system; Section 3 provides the detailed mathematical model formulation used to simulate each components of the system. Section 4 talks about the results of the dynamic simulation and the one-year period case studies. Finally, Section 5 summarizes the main conclusions of the work.

2. Proposed System Overview

This section briefly describes the proposed nuclear hybrid energy system with hydrogen generation and a hydrogen gas turbine. The nuclear hybrid energy system proposed in this study is shown schematically in Figure 1. The proposed system is divided into five different subsystems: (1) NuScale small modular reactor (SMR) module, (2) a steam Rankine power cycle, (3) an underground hydrogen storage, (4) a polymer electrolyte membrane (PEM) electrolyzer, and (5) a hydrogen gas turbine.

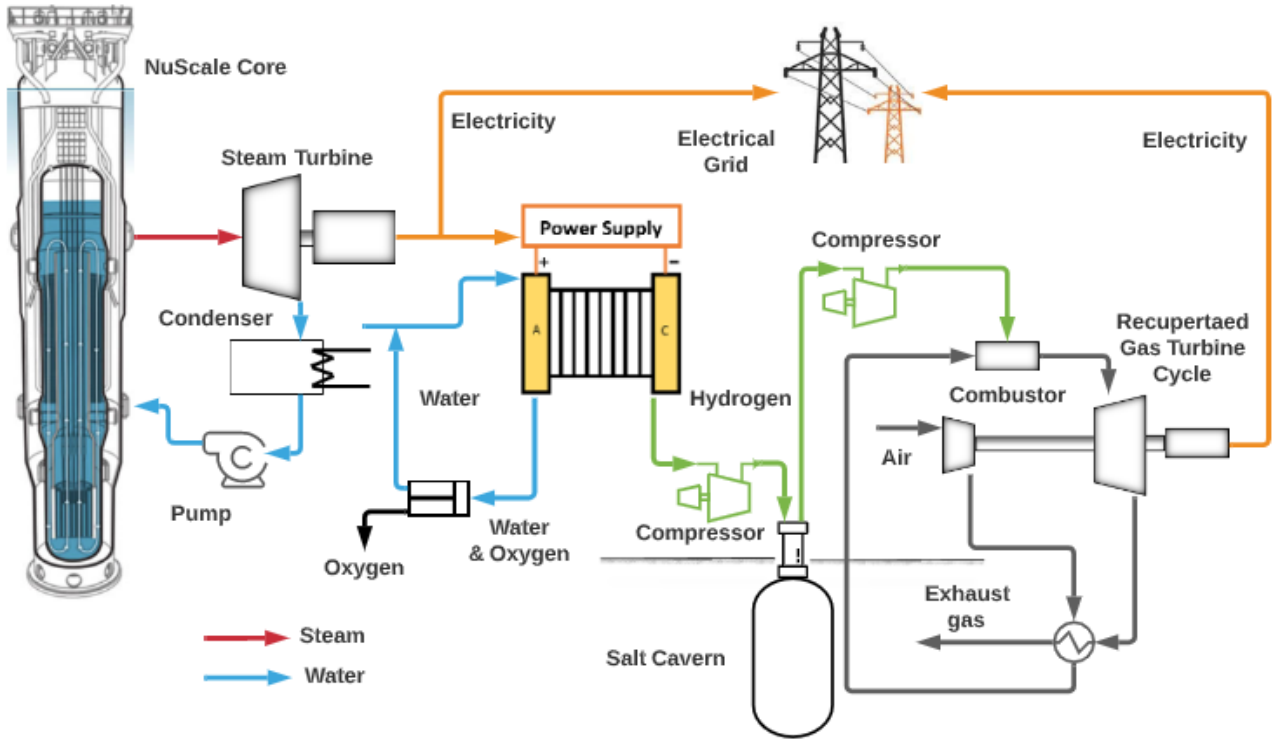

Figure 1. Schematic diagram of the proposed NHES.

In the proposed hybrid energy system, the primary heat generation system is a NuScale small modular reactor (SMR) module. The NuScale SMR is a pressurized light water reactor (LWR) that can consist of up to 12 independently operating modules [32]. The module consists of the nuclear core, a primary loop, a secondary loop and a helical coil steam generator. A NuScale module core has a nominal thermal capacity of 160 MW, with the capability of changing the thermal output by changing the control rods position. By inserting the control rods into the nuclear core, the thermal output capacity can be reduced, and by withdrawing the control rods out of the core, the thermal output capacity can be increased. The primary loop contains the reactor coolant (which is also the moderator) which carries the heat generated in the core, subsequently maintaining the temperature of the core. This coolant also carries the heat from the core to the helical coil steam generator. The coolant, heated by the nuclear core, rises up through the hot leg riser through the steam generator. The hot water is cooled by the heat exchange with water in the secondary loop. As it cools, the coolant is circulated downward until it reaches the core again. The loop is repeated as the coolant is heated up at the core and rises again. This flow is entirely maintained by natural buoyancy forces.

Superheated steam is generated in the secondary loop through the helical coil steam generator. Feed water is pumped into the tubes, where it is heated by the primary loop as it goes up through the steam generator, and comes out as superheated steam. The superheated steam is then distributed to the steam Rankine power cycle to produce electricity. The nominal capacity of the steam Rankine cycle is 49.95 MWe. Low-pressure steam exiting the turbine is condensed in a condenser and pumped back into the steam generator. The electricity produced by the Rankine cycle is distributed to the electrical grid to meet the demand from the grid, and also the demand of the energy storage element, which includes the energy required to drive the hydrogen electrolyzer and the hydrogen compressors.

The energy storage element consists of a hydrogen electrolyzer facility, a multi-stage compressor, and a salt cavern. When the electrical demand is low, the extra energy is used to generate hydrogen through the hydrogen electrolyzer, which is then compressed and pumped into the salt cavern for storage. The hydrogen electrolyzer facility is a large scale, central facility that uses electricity from the steam Rankine cycle to split water into hydrogen and oxygen. In this study, a PEM electrolyzer is used due to its advantages compared to other alkaline electrolysis systems [33]. A multi-staged compressor system, including five compressors, is used to compress the hydrogen into the salt cavern. The first stage compresses the hydrogen from the atmospheric pressure to 2 MPa. Then the next 4 stages of the compressors compress the hydrogen from 2 MPa to 17 MPa, which is the maximum pressure of the salt cavern. For the purpose of this paper, the electrical requirement of the energy storage system consists of the electricity needed to split the water and produce hydrogen, and compress the hydrogen into the underground salt cavern.

The hydrogen generated and stored in the electrolyzer and salt cavern is used to generate additional electricity using a recuperative hydrogen gas turbine cycle. There is currently no

commercially pure hydrogen gas turbine in operation. However, there are many companies working towards 100% hydrogen thermal gas turbines, such as such as Mitsubishi, Siemens, General Electrics, etc. as well as electricity companies preparing to transition to 100% hydrogen fuel in the next decade [34]. When the grid demand is higher than the nominal capacity of the steam turbine, the hydrogen is taken out of the salt cavern, decompressed to compressor outlet pressure, and burned in the gas turbine to suppl [35]y additional electricity to the electrical grid. The system is able to refuel itself and does not require other sources of hydrogen generation.

3. Theoretical model

A theoretical model based on the first law of thermodynamics, as well as mass and energy balances were developed for each components of the Nuclear Hybrid Energy system. The developed model was implemented and simulated in Matlab/Simulink [35].

3.1 The nuclear reactor

The dynamic model for the nuclear reactor was adopted from [36]. The following assumptions were made for the modeling of the nuclear reactor [36]:

- The dynamic model of the reactor is based on the point kinetics equations
- The reactor is assumed to be spatially homogenous
- A single group of delayed neutrons is assumed
- The elements of the reactor consist of the fuel, the moderator, and the control rods
- The effect of control rods position on reactivity is assumed to be quadratic [36]
- The mass flow rate of the coolant is assumed to be constant [37]
- The reactivity dependence on the fuel and moderator temperature are assumed to be linear
- The heat loss of the reactor is assumed to be negligible

The input of the model is the control rods position, measured in meters. The length is correlated to the model that is used, so that it can be used to access the impact on the neutronics more clearly. The output of the model is the thermal power of the nuclear reactor ($MWth$) as well as the temperature of the moderator and the fuel.

Neutron dynamics model of the reactor:

The neutron dynamics model was taken from [38]:

$$\frac{dn_{neu}}{dt} = \frac{\rho_{nuc}(t) - \beta_{mix}}{\Lambda} n_{neu}(t) + \lambda C_{neu}(t) \quad (1)$$

$$\frac{dC_{neu}}{dt} = \frac{\beta_{mix}}{\Lambda} n_{neu}(t) - \lambda C_{neu}(t) \quad (2)$$

where n is the neutron density, $\rho(t)$ is reactivity, β_{mix} is the effective delayed neutron fraction, Λ is the neutron generation time, λ is the decay constant for the single average group of delayed neutrons, $C(t)$ is the concentration of the single average group of delayed neutrons. The values of β_{mix}, λ, and Λ are given in Table 1.

Table 1
The values for the parameters in the neutron dynamic model.

Parameter (unit)	Value
β_{mix}	0.0065
$\lambda(s^{-1})$	0.07728
$\Lambda(\mathrm{s})$	2.18×10^{-5}

The reactivity of the reactor is modelled using the following equation:

$$\rho_{nuc}(t) = \alpha_f(T_f - T_{f0}) + \alpha_m(T_m - T_{m0}) + p_2 z^2 + p_1 z + p_0 \quad (3)$$

where T_f is the fuel temperature, T_m is the moderator temperature, T_{f0} and T_{m0} are the reference temperature of fuel and moderator respectively, α_f is the fuel temperature feedback coefficient, α_m is the moderator temperature feedback coefficient, z is the control rods position measured in meters, $p_2 z^2 + p_1 z + p_0$ describes the effect of the control rods position to the reactivity. The values for the feedback coefficients are taken from [39] which is specifically for a NuScale reactor. The values for p_2, p_1, p_0 are taken from [36], which is for a pressurized water reactor. The values for these parameters are given in Table 2.

Table 2
Values of parameters for reactivity calculation.

Parameter (unit)	Value
$\alpha_f(\Delta k/k/°\mathrm{C})$	-1.98×10^{-5}
$\alpha_m(\Delta k/k/°\mathrm{C})$	-28.2×10^{-5}
p_2	-0.966
p_1	-0.44
p_0	0.0401

Thermodynamic equations of the reactor:

To model the temperature of the fuel and coolant, energy balances are used. The energy balance on the fuel rods is as follow:

$$\frac{dT_f}{dt} = -\frac{hA_s}{\rho_f V_f C_{pf}}(T_f - T_m) + \frac{W_{therm}}{\rho_f V_f C_{pf}} \quad (4)$$

where ρ_f is the fuel density, V_f is the fuel volume, C_{pf} is the heat capacity of the fuel, W_{therm} is the thermal power generated from the fuel, h is the convective heat transfer coefficient from the fuel to the coolant, A_s is the surface area between the fuel and the coolant, $\rho_f V_f C_{pf} \frac{dT_f}{dt}$ describes the inner energy change of the fuel due to temperature change, and $hA_s(T_f - T_m)$ describes the transferred heat from the fuel to the coolant.

The energy balance on the coolant is:

$$\frac{dT_m}{dt} = \frac{hA_s}{\rho_m V_m C_{pm}}(T_f - T_m) - \frac{\dot{m}_m}{\rho_m V_m}(T_m - T_{m,in}) \quad (5)$$

where ρ_m is the coolant density, V_m is the coolant volume, C_{pm} is the heat capacity of the coolant, $\rho_m V_m C_{pm} \frac{dT_m}{dt}$ describes the inner energy change of the coolant due to temperature change, m_p is the coolant mass flow rate, $T_{m,in}$ is the coolant inlet temperature.

The thermal power of the reactor is related to the neutron density as follows [40]:

$$W_{therm} = n(t)\, \sigma_f^{235}\, E_f\, N_{235} V_{core} \tag{6}$$

where E_f is the average recoverable energy per fission, σ_f^{235} is the microscopic cross section of Uranium 235, N_{235} is the atomic number density of Uranium 235 in the fuel, V_{core} is the total volume of the core.

The convective heat transfer is calculated using the Dittus-Boelter correlation [41]:

$$h_{conv} = \frac{Nu_{Dh}\, \kappa_m}{Dh} \tag{7}$$

$$Nu_{Dh} = 0.023\, Re_{Dh}^{0.8} Pr^{0.4} \tag{8}$$

where κ_m is the thermal conductivity of the coolant, Dh is the hydraulic diameter (m), Re is the Reynolds number of the flow, Pr is the Prandtl number, and Nu is the Nusselt number.

Steam generator

A steady-state energy balance on the steam generator is used:

$$\dot{m}_{steam} \Delta H_{steam} = \dot{m}_m C_{pm} \left(T_{m,in} - T_{m,out}\right) \tag{9}$$

The nominal value of steam flow rate is 67.6 kg/s at 580.9 K. According to [37], it is assumed that the steam generator exit temperature is constant. As the power output of the nuclear reactor changes, so does the temperature of the coolant. The amount of steam is calculated with new values of coolant temperature.

Steam Rankine cycle

The Rankine Cycle is modeled using pseudo-steady-state energy models. The power generated by the turbine is calculated using the following steady-state equation:

$$\dot{W}_{turb} = \dot{m}_{steam} \left(H_{turb,in} - H_{turb,out}\right) \tag{10}$$

Assuming that the turbine isentropic efficiency is constant, the enthalpy of the outlet steam of the turbine is calculated using Eq. (11) as follows:

$$H_{turb,out} = H_{turb,in} + \eta_{turb} \left(H_{turb-is,out} - H_{turb,in}\right) \tag{11}$$

where $H_{turb-is,out}$ is the isentropic (ideal) outlet enthalpy of the steam.

The power needed for the pump is calculated using Eq. (12) as follows:

$$\dot{W}_{pump} = \dot{m}_{steam} \widehat{V}_s \left(P_{pump,out} - P_{pump,in}\right) \tag{12}$$

where $\widehat{V}_s$ is the specific volume of water at the pump inlet conditions. $P_{pump,out}$ is the pressure at the outlet of the pump, and $P_{pump,in}$ is the pressure at the inlet of the pump.

3.2 Hydrogen generation

Hydrogen is generated by using extra energy during low demand time by using a PEM water electrolyzer process. An electrochemical model of the electrolyzer is developed to calculate the amount of hydrogen produced as a function of power. The electrolyzer has four subsystems of the anode, the cathode, the membrane, and the voltage. The developed model for the PEM electrolyzer is adapted from [42] and [43].

3.2.1 Anode Module

The half-cell reaction taking place inside the anode is:

$$2H_2O \rightarrow O_2 + 4H^+ + 4e^- \tag{13}$$

The oxygen flow rate is calculated as:

$$\dot{N}_{O_2} = \dot{N}_{O_2,an,in} - \dot{N}_{O_2,an,out} + \dot{N}_{O_2,gen} \tag{14}$$

$$\dot{N}_{O_2,gen} = \frac{I}{4F} \tag{15}$$

where I is the current, and F is Faraday's constant.

The oxygen molar flow rate per area is:

$$\dot{n}_{O_2} = \frac{\dot{N}_{O_2}}{A} \tag{16}$$

where A is the area of the membrane-electrode-assembly.

The water flow rate through the anode is the water consumed by the reaction as well as the water transported to the other side of the membrane:

$$\dot{N}_{H_2O,an} = \dot{N}_{H_2O,mem} + \dot{N}_{H_2O,cons} \tag{17}$$

$$\dot{N}_{H_2O,cons} = \frac{I}{2F} \tag{18}$$

The water molar flow rate per area at the anode is:

$$\dot{n}_{H_2O,an} = \frac{\dot{N}_{H_2O,an}}{A} \tag{19}$$

The molar flow rate of each species at the anode allows us to calculate the molar fraction of each species inside the anode:

$$y_{O_2,an} = \frac{\dot{n}_{O_2}}{\dot{n}_{O_2} + \dot{n}_{H_2O,an}} \tag{20}$$

$$y_{H_2O,an} = \frac{\dot{n}_{H_2O,an}}{\dot{n}_{O_2} + \dot{n}_{H_2O,an}} \tag{21}$$

With these molar fractions, the concentrations and partial pressure at the anode are:

$$C_{O_2,an} = \frac{P_{an} y_{O_2,an}}{RT_{an}} \tag{22}$$

Applying Fick's law, the concentration at the membrane-anode interface can be calculated:

$$C_{O_2,mem} = C_{O_2,an} + \frac{\delta_{e,an}}{D_{eff,an}}\, \dot{n}_{O_2} \tag{23}$$

where $\delta_{e,an}$ is the anode thickness, and $D_{eff,an}$ is the effective diffusion coefficient at the anode. This diffusion coefficient is calculated in the membrane module.

The molar fractions are calculated at the membrane-anode interface:

$$y_{O_2,mem} = \frac{RT_{an}}{P_{an}} C_{O_2,mem} \tag{24}$$

Then the partial pressures can be calculated as:

$$P_{O_2,mem} = y_{O_2,mem}\, P_{an} \tag{25}$$

3.2.2 Cathode module

The half-cell reaction taking place at the cathode module is:

$$4H^+ + 4e^- \rightarrow 2H_2 \tag{26}$$

The hydrogen flow rate inside the cathode is calculated as:

$$\dot{N}_{H_2} = \dot{N}_{H_2,cat,in} - \dot{N}_{H_2,cat,out} + \dot{N}_{H_2,gen} \tag{27}$$

$$\dot{N}_{H_{2,gen}} = \frac{I}{2F} \tag{28}$$

The hydrogen molar flow rate per area is:

$$\dot{n}_H = \frac{\dot{N}_{H_2}}{A} \tag{29}$$

The water flow rate inside the cathode is the amount of water flowing from the anode through the membrane to the cathode:

$$\dot{N}_{H_2O,cat} = \dot{N}_{H_2O,mem} \tag{30}$$

The water molar flow rate per area at the cathode is:

$$\dot{n}_{H_2O,cat} = \frac{\dot{N}_{H_2O,cat}}{A} \tag{31}$$

Like the anode, the molar fractions of each species inside the cathode are:

$$y_{H_2,cat} = \frac{\dot{n}_{H_2}}{\dot{n}_{H_2} + \dot{n}_{H_2O,cat}} \tag{32}$$

$$y_{H_2O,an} = \frac{\dot{n}_{H_2O,cat}}{\dot{n}_H + \dot{n}_{H_2O,cat}} \tag{33}$$

which can then be used to calculate the concentration of each species inside the cathode:

$$C_{H_2,cat} = \frac{P_{cat} y_{H_2,cat}}{RT_{cat}} \tag{34}$$

where the molar fraction of each species inside the cathode is calculated using Fick's law:

$$C_{H_2,mem} = C_{H_2,cat} + \frac{\delta_{e,cat}}{D_{eff,cat}} \dot{n}_{H_2} \tag{35}$$

where $\delta_{e,cat}$ is the cathode thickness, and $D_{eff,cat}$ is the effective diffusion coefficient at the cathode. This diffusion coefficient is calculated in the membrane module.

The molar fractions at the membrane-anode interface can be calculated:

$$y_{H_2,mem} = \frac{RT_{cat}}{P_{cat}} C_{H_2,mem} \tag{36}$$

Then the partial pressures can be calculated as:

$$P_{H_2,mem} = y_{H_2,mem} P_{cat} \tag{37}$$

3.2.3 Membrane module

The membrane module describes the transport of water through the membrane. The water moves through the membrane through electro osmotic drag and diffusion. The electro osmotic drag happens as the H^+ ions moving through the membrane and drags some water molecules with them. The amount of water dragged through this phenomenon is described as:

$$\dot{N}_{H_2O,eod} = \frac{n_d I}{F} \tag{38}$$

where n_d is the electro-osmotic drag coefficient, in units of mol_{H_2O}/mol_{H^+}.

The diffusion of water due to the presence of water concentration gradient can be calculated as:

$$\dot{N}_{H_2O,diff} = D_w \left(\frac{C_{H_2O,mem,cat} - C_{H_2O,mem,an}}{t_{me}} \right) MW_{H_2O} A \tag{39}$$

where $C_{H_2O,mem,cat}$ and $C_{H_2O,mem,an}$ are the water concentration at the membrane on the cathode and anode side respectively. t_{me} is the thickness of the membrane, D_w is the diffusion coefficient of water, and A is the area. The water concentration at both sides of the membrane can be calculated as a function of the water concentration in the electrode channel. Using Fick's law of diffusion:

$$C_{H_2O,mem,cat} = C_{H_2O,cat} + \frac{\delta_{e,cat}}{D_{eff,cat}} \dot{n}_{H_2O,cat} \tag{40}$$

$$C_{H_2O,mem,an} = C_{H_2O,an} + \frac{\delta_{e,an}}{D_{eff,an}} \dot{n}_{H_2O,an} \tag{41}$$

where $D_{eff,an}$ and $D_{eff,cat}$ are, respectively, the O_2/H_2O and the H_2/H_2O effective binary diffusion coefficients. They can be calculated by using the porosity correction applied to the diffusion coefficients. The following correlation [44] is used:

$$D_{eff,\ A-B} = D_{A-B} \epsilon \left(\frac{\epsilon - \epsilon_p}{1 - \epsilon_p} \right)^{\alpha} \tag{42}$$

where ϵ is the porosity of electrodes, ϵ_p is the percolation threshold, α is an empirical coefficient. The values used to calculate these parameters are presented in Table 3 [45] [46] [47] [48].

Table 3

Values to calculate effective binary diffusion coefficients

Coefficient	Value
ϵ	0.3
ϵ_p	0.11
α	0.785

D_{A-B} is the binary diffusion coefficient for species A and B, which can be calculated using Eq. (43) as follows:

$$P D_{A-B} = a \left(\frac{T}{\sqrt{T_{c,A} T_{c,B}}} \right)^{b} \left(P_{c,A} P_{c,B} \right)^{\frac{1}{3}} \left(T_{c,A} T_{c,B} \right)^{\frac{5}{12}} \left(\frac{1}{MW_A} + \frac{1}{MW_B} \right)^{\frac{1}{2}} \tag{43}$$

where P is pressure in atm, T is temperature in K. Also, a and b are dimensionless empirical coefficients, with values given in Table 4.

Table 4

Values for dimensionless coefficients for the calculations of binary coefficients for species A and B.

Coefficients	Pairs of two nonpolar gases	Pairs of H_2O and a nonpolar gas

a	2.745×10^{-4}	3.640×10^{-4}
b	1.823	2.334

T_c, P_c, MW are the critical temperature, pressure and molecular weight of species A and B with values for H_2, O_2, and H_2O in Table 5.

Table 5
Critical temperature, pressure and molecular weight for hydrogen, oxygen and water.

	H_2	O_2	H_2O
$P_c(atm)$	12.8	49.7	218.3
$T_c(K)$	33.3	154.4	647.3
$MW(g/mol)$	2	32	18

The concentration of water at the electrodes can be calculated as:

$$C_{H_2O,an} = \frac{\rho_{H_2O}(T_{an})}{MW_{mem,H_2O}} \tag{44}$$

$$C_{H_2O,cat} = \frac{\rho_{H_2O}(T_{cat})}{MW_{mem,H_2O}} \tag{45}$$

The net water flow through the membrane can now be calculated as:

$$\dot{N}_{H_2O,mem} = \dot{N}_{H_2O,eod} + \dot{N}_{H_2O,diff} \tag{46}$$

The water molar fraction and pressure inside the membrane for cathode and anode can be calculated using Eqs. (47)-(48) and (49)-(50), respectively:

$$y_{H_2O,mem,cat} = \frac{C_{H_2O,mem,cat}}{C_{H_2O,mem,cat} + C_{H_2,mem}} \tag{47}$$

$$P_{H_2O,mem,cat} = y_{H_2O,mem,cat} P_{cat} \tag{48}$$

$$y_{H_2O,mem,an} = \frac{C_{H_2O,mem,an}}{C_{H_2O,mem,an} + C_{O_2,mem}} \tag{49}$$

$$P_{H_2O,mem,an} = y_{H_2O,mem,an} P_{an} \tag{50}$$

3.2.4 Voltage module

The real cell voltage in an electrolyzer is higher than the ideal open-circuit voltage, and can be expressed as:

$$Vol = E + \eta_{act} + \eta_{ohm} \tag{51}$$

where Vol is the real cell voltage, E is the ideal open circuit voltage, η_{act} is the activation overvoltage, and η_{ohm} is the Ohmic overvoltage. The calculations of each term are presented by Eqs. (52)-(56).

Open circuit voltage is calculated by using the Nernst equation:

$$E = E_{rev}^0 + \frac{RT}{2F}\left[\ln\left(\frac{P_{H_2} P_{O_2}^{\frac{1}{2}}}{P_{H_2O}}\right)\right] \tag{52}$$

where E_{rev}^{0} is the reversible cell potential at standard temperature and pressure. It is modeled by an empirical temperature dependence equation:

$$E_{rev}^{0} = 1.229 - 0.9 \times 10^{-3}(T - 298) \tag{53}$$

Activation overpotential is calculated as the sum of the activation overpotential on both the anode and the cathode side, as presented by Eqs. (54)-(56).

$$V_{act,an} = \frac{RT_{an}}{\alpha_{an}F}\operatorname{arcsinh}\left(\frac{i}{2i_{0,an}}\right) \tag{54}$$

$$V_{act,cat} = \frac{RT_{cat}}{\alpha_{cat}F}\operatorname{arcsinh}\left(\frac{i}{2i_{0,cat}}\right) \tag{55}$$

$$\eta_{act} = V_{act,an} + V_{act,cat} \tag{56}$$

where $i_{0,an}$ and $i_{0,cat}$ are the exchange current density at anode and cathode electrodes, respectively, and α_{an} and α_{cat} are the charge transfer coefficients at anode and cathode electrodes, respectively. The values for these parameters are given in Table 6.

Table 6

Parameters to calculate activation overpotential.

	Anode	Cathode
i_0	2×10^{-7}	2×10^{-3}
α	2	0.5

Ohmic overpotential can be calculated using Eqs. (57)-(59) as follows:

$$\eta_{ohm} = i\, R_{ohm} \tag{57}$$

$$R_{ohm} = \frac{t_{me}}{\sigma_{me}} \tag{58}$$

$$\sigma_{me} = (0.01539\,\lambda - 0.00326)\exp\left[1268\left(\frac{1}{303} - \frac{1}{T}\right)\right] \tag{59}$$

where t_{me} is the membrane thickness, σ_{me} is the material conductivity, i is the current density of the electrolyzer, T is the temperature of the electrolyzer, and λ is the membrane water content.

3.2.5 Efficiency

The efficiency of the electrolyzer is calculated using Eq. (60) as follows:

$$\eta_{elec} = \frac{P_{Ideal}}{P_{actual}} \times 100\% \tag{60}$$

From [49], the ideal amount of power to generate 1 kg of hydrogen is 39 kWh. The actual amount of power can be calculated by Eq. (61):

$$P_{actual} = I\,V \tag{61}$$

where I is the current and V is the voltage.

3.3 Salt Cavern Model

The salt cavern model is composed of the material balance and energy balance inside the cavern, as presented by Eqs. (62) and (63):

$$\frac{dn_{H_2}}{dt} = \dot{N}_{H_2,in} - \dot{N}_{H_2,out} \tag{62}$$

$$n_{H_2}\frac{dT_{cav}}{dt} = \frac{\dot{N}_{H_2,in}\,C_{p,in}T_{in} + h_{cav}(T_w - T_{cav}) - \dot{N}_{H_2,out}\,C_{p,out}T_{out}}{C_{p,H_2} - T_{cav}\dfrac{dn_{H_2}}{dt}} \tag{63}$$

where h_{cav} is the convective heat transfer coefficient between the hydrogen gas inside the cavern and the wall of the cavern. T_w is the temperature of the wall, and T is the temperature of the hydrogen gas inside the cavern. The convective heat transfer coefficient is calculated using the correlation used by [50].

The pressure of the cavern can be calculated at each time step with:

$$P_{cav} = \frac{z_{comp}n_{H_2}RT_{cav}}{V_{cav}} \tag{64}$$

where z_{comp} is the compressibility factor of hydrogen, which can be calculated at each time step with the following correlation [51]:

$$z(P,T) = 1 + \sum_{i=1}^{9} a_i \left(\frac{100K}{T}\right)^{b_i}\left(\frac{P}{1MPa}\right)^{c_i} \tag{65}$$

where a_i, b_i, and c_i are constant coefficients, which can be found in [46].

To pump hydrogen into the salt cavern, hydrogen is compressed to a pressure that is higher than the pressure of the salt cavern. The thermodynamic parameters of compressing this hydrogen are taken from [52]. The amount of power needed to compress the hydrogen produced is:

$$W_{comp} = \dot{N}_{H_2}\left[H_{H_2}\left(P_{comp,out}, T_{comp,out}\right) - H_{H_2}\left(P_{comp,in}, T_{comp,in}\right)\right] \tag{66}$$

where $H_{H_2}\left(P_{comp,out}, T_{comp,out}\right)$ is the enthalpy of hydrogen at the outlet pressure and temperature of the compressor, and $H_{H_2}\left(P_{comp,in}, T_{comp,in}\right)$ is the enthalpy of hydrogen at the inlet pressure and temperature of the compressor.

The salt cavern has a minimum and maximum pressure threshold. These thresholds are needed to maintain geotechnical safety of the salt cavern. The lower bound pressure limit is to help maintain the capability for gas injection as well as gas withdrawal [23]. It also makes sure that the cavern salt cavern is stable and will not cave in [26]. The maximum pressure limit is to prevent the salt cavern from rock fracturing, resulting from the high pressure on the cavern wall [53]. The minimum and maximum cavern pressure can be calculated as follows:

$$P_{min} = 0.24(P_{overburden}) \tag{67}$$

$$P_{max} = 0.80(P_{overburden}) \tag{68}$$

$$P_{overburden} = \rho_{rock}\, g\, (D - H) \tag{69}$$

where P_{min} is the minimum pressure of the salt cavern, P_{max} is the maximum pressure of the salt cavern. $P_{overburden}$ is the overburden pressure, or sometimes called lithostatic pressure. ρ_{rock} is the density of the rock in $kg\ m^{-3}$, g is the gravitational acceleration (assumed as 9.81 $m\ s^{-2}$), D is the cavern depth in m, and H is the cavern height in meters.

3.4 Brayton Cycle Model

During peak demand times, hydrogen can be taken out of the cavern and burned in a gas turbine to produce electricity for the grid. The gas turbine model comprises of a compressor,

combustion chamber, turbine, generator, and recuperator. The thermodynamics model was adapted from [8] and [54].

The compressor can be modeled as:

$$T_{comp,out} = T_{amb}\left(1 + \frac{x_c - 1}{\eta_{comp}}\right) \tag{70}$$

$$x_c = \left(\frac{PR_c \dot{m}_a}{\dot{m}_{a,nom}}\right)^{\frac{\gamma_{c-1}}{\gamma_c}} \tag{71}$$

where $T_{comp,out}$ is the outlet temperature of the compressor, T_{amb} is the ambient temperature, which can be used as inlet temperature of the compressor, η_{comp} is the efficiency of the compressor, PR_c is the compressions ratio, $\dot{m}_{a,nom}$ is the nominal intake air flow rate, and γ_c is the cold end ratio of specific heats. The air flow rate can be calculated using:

$$\dot{m}_a = \frac{P_{amb}}{P_{amb,o}}\sqrt{\frac{T_{amb,o}}{T_{amb}}}\frac{\sin(\theta_{IGV} - \theta_{min})}{\sin(\theta_{max} - \theta_{min})}\dot{m}_{a,nom} \tag{72}$$

where P_{amb} is the ambient pressure, $P_{amb,o}$ is the ambient reference pressure, $T_{amb,o}$ is the ambient reference temperature, θ_{IGV} is the angle of the IGVs, θ_{min} and θ_{max} are the minimum and maximum IGV angles respectively.

For the combustion chamber model, the turbine firing temperature, which is the exit temperature of the combustion chamber, can be modeled using Eq. (73) as follows:

$$T_{fire} = T_{comp,in} + \left(\frac{\eta_{comb} LHV}{C_{p,e}}\right)\left(\frac{\dot{m}_f}{\dot{m}_f + \dot{m}_a}\right) \tag{73}$$

where $T_{comp,in}$ is the temperature going into the compressor, $\dot{m}_f$ is the fuel (hydrogen) flow rate, η_{comb} is the combustion efficiency, LHV is the lower heating value of hydrogen, and $C_{p,e}$ is the specific heat of the exhaust gas flow.

The turbine exhaust temperature can be modeled by relating it to the firing temperature in the following equation:

$$T_e = T_f\left(1 - \left(1 - \frac{1}{x_h}\right)\eta_{turb}\right) \tag{74}$$

$$x_h = \left(PR_T \frac{\dot{m}_f + \dot{m}_a}{\dot{m}_{f,nom} + \dot{m}_{a,nom}}\right)^{\frac{\gamma_h - 1}{\gamma_h}} \tag{75}$$

T_e is the turbine exhaust temperature, η_{turb} is the turbine efficiency, $\dot{m}_{f,nom}$ is the nominal fuel flow, and γ_h is the hot end ratio of the specific heats. From these temperatures, the steady state power generation of the plant can be calculated:

$$W_{GasTurb} = (\dot{m}_f + \dot{m}_a)C_{p,h}(T_f - T_e) - \dot{m}_a C_{p,a}(T_d - T_{amb}) \tag{76}$$

where $C_{p,a}$ is the heat capacity of air, which is assumed to be constant for this model.

The recuperation is modeled as follows:

$$T_{comp,in} = \eta_{recup}(T_e - T_{comp,out}) + T_{comp,out} \tag{77}$$

$$T_{recup} = \frac{T_e - \dot{m}_a C_{p,a}(T_{c,in} - T_d)}{(\dot{m}_f + \dot{m}_a) C_{p,h}} \tag{78}$$

where η_{recup} is the efficiency of the recuperator, assumed at 75%. T_{recup} is the outlet temperature of the recuperator.

The efficiency of the Brayton cycle can be calculated by Eq. (79) as follows:

$$\eta_{Brayton} = \frac{P_{overall}}{\dot{m}_f LHV} \times 100\% \tag{79}$$

3.5 System Controls

A detailed control scheme of the proposed NHES is shown schematically in Figure 2.

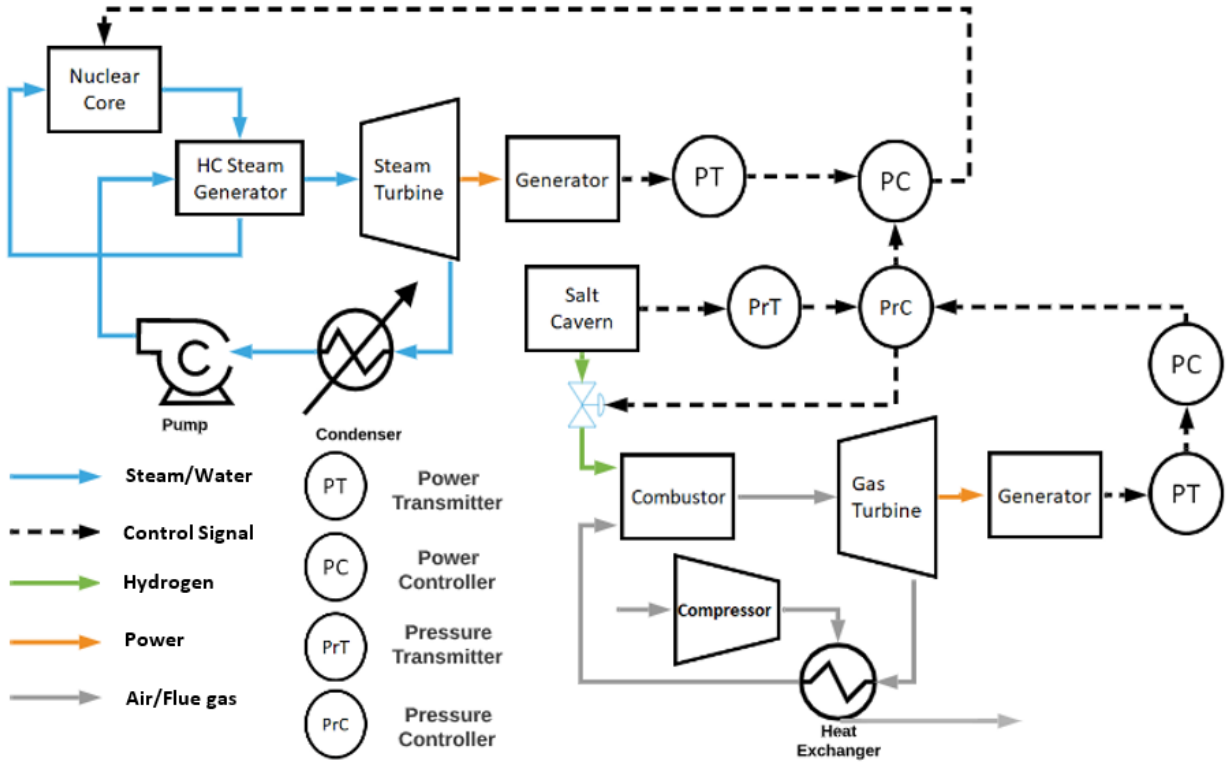

Figure 2. The control scheme of the proposed NHES.

PI controllers regulate the power output of the steam Rankine cycle as well as the gas turbine cycle. To moderate the power output of the steam Rankine cycle, the pressure inside the salt cavern is directly measured through a pressure sensor (PrT in Figure 2). When the pressure inside the salt cavern reaches its maximum limit, the hydrogen generation is stopped. If the grid demand is lower than the nominal capacity of the steam Rankine cycle, the power output of the steam Rankine cycle is ramped down and match with the grid demand by changing the control rods position. If the grid demand is higher than the nominal capacity of the steam Rankine cycle, no action needs to be taken, as there is no excess electricity used to generate hydrogen. This way, it is ensured that the salt cavern will operate within its safety conditions.

When the demand is higher than the nominal capacity of the steam Rankine cycle, the rest of the demand can be met with by the hydrogen gas turbine. The difference between the grid

demand and the steam cycle nominal capacity is the gas turbine set point. If the grid demand is lower than the steam cycle nominal capacity, the gas turbine set point is set to zero. The controller for the gas turbine will moderate the power output by changing the amount of hydrogen needed for fuel. There is also a pressure sensor for this controller. When the pressure inside the salt cavern reaches the minimum pressure threshold, the controller would shut down the gas turbine.

3.6 Model Validation

This section presents the validation results for different subsystems of the hybrid energy system. Note that for the steam Rankine cycle, the model has been validated previously in [55] and the validation results are not presented here.

3.5.1 NuScale power plant

To validate the developed model for the nuclear core, the results of this study are compared against those presented in the study of Gabor et al. [36] using the following input parameters presented in Table 7:

Table 7

Input parameter used for nuclear core model.

Parameter (unit)	Value
$\alpha_f (\$/°C)$	-5.326×10^{-3}
$\alpha_m (\$/°C)$	-2.018×10^{-2}
$\phi_0\ (cm^{-2}s^{-1})$	1.3018×10^{13}
$\sigma_X\ (cm^2)$	2.8041×10^{-18}

Table 8 shows the validation results in terms of neutron flux (%) and moderator temperature for different control rods positions. As can be seen, the results of this study show a very good agreement with those of Gabor et al. [36].

Table 8

Validation results for the reactor core.

Control Rods Position (m)	Neutron Flux (%)		Moderator Temperature (^{0}C)	
	This study	Gabor et al. [36]	This study	Gabor et al. [36]
0	100	100	280.2	280.2
0.18	97.5	96.1	279.3	278.5
0.25	94.0	93.1	278.5	278

3.5.2 Electrolyzer

The voltage and efficiency of the electrolyzer are used as an indicator to validate the accuracy of the developed electrolyzer model. For these validations, the following input parameters presented in Table 9 were used.

Table 9

Input parameters for hydrogen electrolyzer.

Parameter (unit)	Value
Anode temperature (K)	298.15
Anode pressure (Pa)	101325
Anode thickness (m)	8×10^{-5}

Cathode temperature (K)	298.15
Cathode pressure (Pa)	101325
Cathode thickness (m)	8×10^{-5}
Membrane thickness (m)	0.1756×10^{-5}
Area (m^2)	160×10^{-4}
$D_w(m^2/s)$	1.28×10^{-10}

In terms of voltage, and the results are compared against those presented by [43]. The voltage validation results are presented in Figure 3, showing the variation of voltage with current density. According to Figure 3, the results of this study have a close agreement with those of [43]. The average percentage error between the results of this study and the results of [43] is 1.67%.

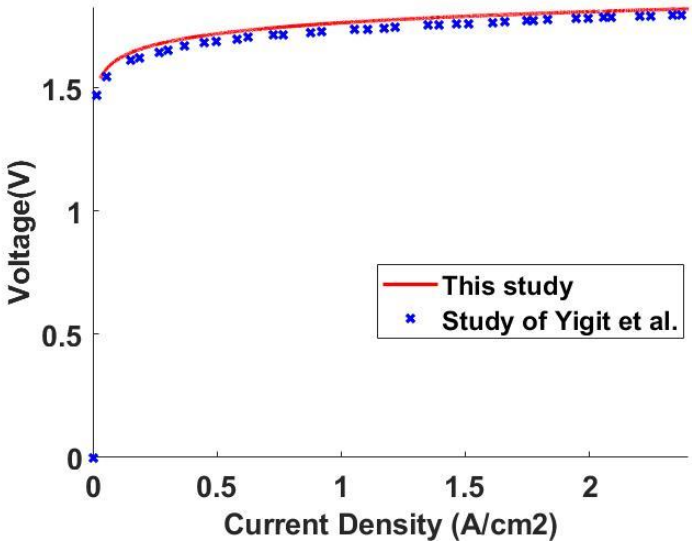

Figure 3. Comparison between the voltage of the proposed model and Yigit et al.'s model *[43]*.

To further validate the model, the efficiency of the electrolyzer is compared with the results found in [43] for different values of current densities and the validation results are presented in Figure 4. It is found that the results of this study are in excellent agreement with those of [43], with an average percentage error of 1.1%.

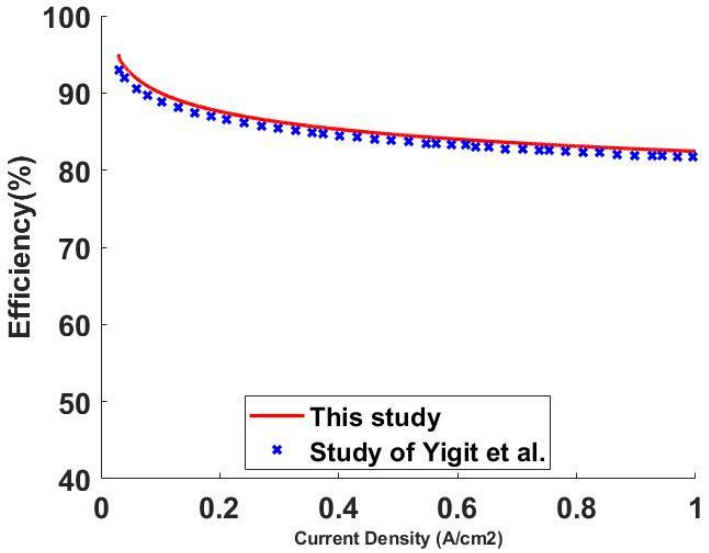

Figure 4. Comparison between the efficiency of the proposed model and Yigit et al's model *[43]*.

3.5.3 Salt Cavern

The results of the developed salt cavern model are compared with the results taken from [56] for the following input parameters given in Table 10. Figure 5 shows the validation results in terms of variation of hydrogen pressure with time. As noticed, the results of this study have an excellent agreement with those presented in [56].

Table 10

Input used to validate the developed salt cavern model.

Input parameter	This study
Initial Pressure (MPa)	2
Initial Temperature (K)	290
Hydrogen compressibility	A function of T and P
Hydrogen dynamic viscosity (Pa·s)	A function of T and P
Volume (m^3)	40,000
Injected/extracted mass flow rate (kg/s)	0.034

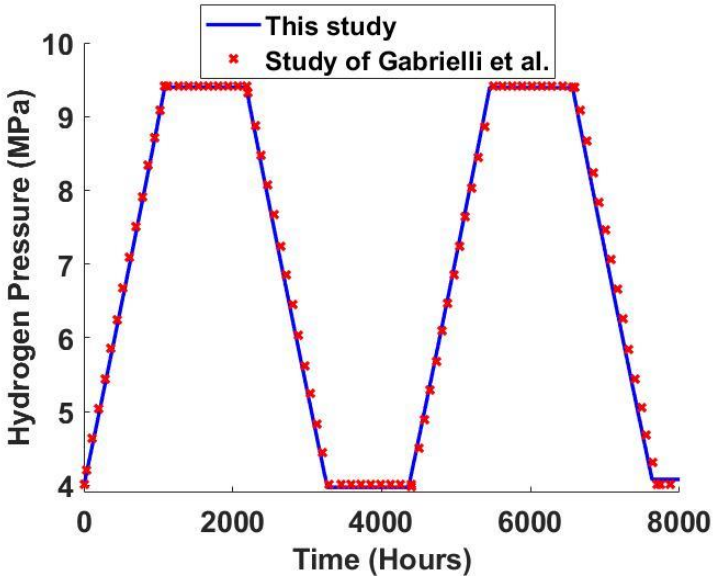

Figure 5. Comparison between the proposed model and Gabrielli et al.'s model *[56]*.

3.5.4 Gas Turbine

Using natural gas as a fuel, the gas turbine cycle model was previously validated in [55]. Since there is no available gas turbine that uses just purely hydrogen as fuel, some assumptions are made in the proposed model. To validate the results using in this model, the hydrogen gas turbine efficiency is compared with the reported efficiency of a mixed natural gas/hydrogen fuel gas turbine efficiency made by Mitsubishi. The recorded efficiency of the Mitsubishi turbine is 63% [57]. The calculated efficiency of the proposed gas turbine cycle (Brayton cycle) when run with a fuel flow of 0.2 kg/s is 55.37%, which is comparable. The reason for a lower performance is that a simple recuperative cycle is used, which is not optimized for the gas turbine. In future work, the system will be optimized to the flow rate and temperature of the gas turbine. The objective of the paper is not to propose a new hydrogen gas turbine, but the overall integration feasibility study of the NHES.

4. Results and Discussions

This section presents the dynamic simulation results of the proposed nuclear hybrid energy system in three different cases: CAISO, ERCOT and ISO NEW ENGLAND. Using the developed model and control schemes, the performance of the proposed NuScale NHES is evaluated by using data from CAISO [58], ERCOT [59], and New England ISO [60] for the system's grid demand, scaled down to the appropriate level. The NHES system is simulated over a one-year period and compared. To compare the results of the proposed hybrid system in the three cases, different performance criteria are chosen. These criteria include nuclear plant capacity factor, total power produced, percentage of total demand met, percentage of time when the demand is met, total number of ramping cycles, standard deviation of the nuclear power output, and the percentage of time needed to ramp up and down.

Nuclear capacity factor is defined as the total output of the nuclear plant divided by the maximum total output of the nuclear plant. This is computed for both the NHES and stand-alone

reactor by integrating the nuclear output over one-year and dividing by the maximum total power output. The total power produced is the total amount of electricity produced by all the electrical generators, which is just the nuclear plant in the case of a stand-alone nuclear plant, but also include the gas turbine output in the hybrid system. This is computed by integrating the total power output for both cases over a one-year period. The percentage of total demand met is calculated as the total power produced divided by the total demand from the grid during the time frame of the study

A full ramping cycle is defined in this paper as when the control rods of the nuclear reactor ramps down to a local minimum and then ramps back up to a local maximum. The total number of ramping cycles reveal how much the nuclear reactor has to ramp up and down and thus can be used to compare the flexible capacity of the two scenarios. The standard deviation of the nuclear power output is computed by finding the standard deviation of the nuclear power output for both systems. This is used to compare the amount of variation of the nuclear output, and thus demonstrate that the proposed NHES reduces the ramping rate. Lastly the percentage of time needed to ramp up and down is the amount of time the NHES and the stand-alone reactor ramp up and down, divided by one year. This criterion is chosen to show the impact on ramping rate the NHES has on a nuclear power plant.

4.1 CAISO Simulation Results

The simulation results for CAISO with 7-day rolling average are presented in figure 6 (a)-(c). The results presented in Figure 6 are as follows: 6 (a): the power output of the NHES, 6 (b): the control rods position of the nuclear reactor, and 6 (c): the pressure inside the salt cavern.

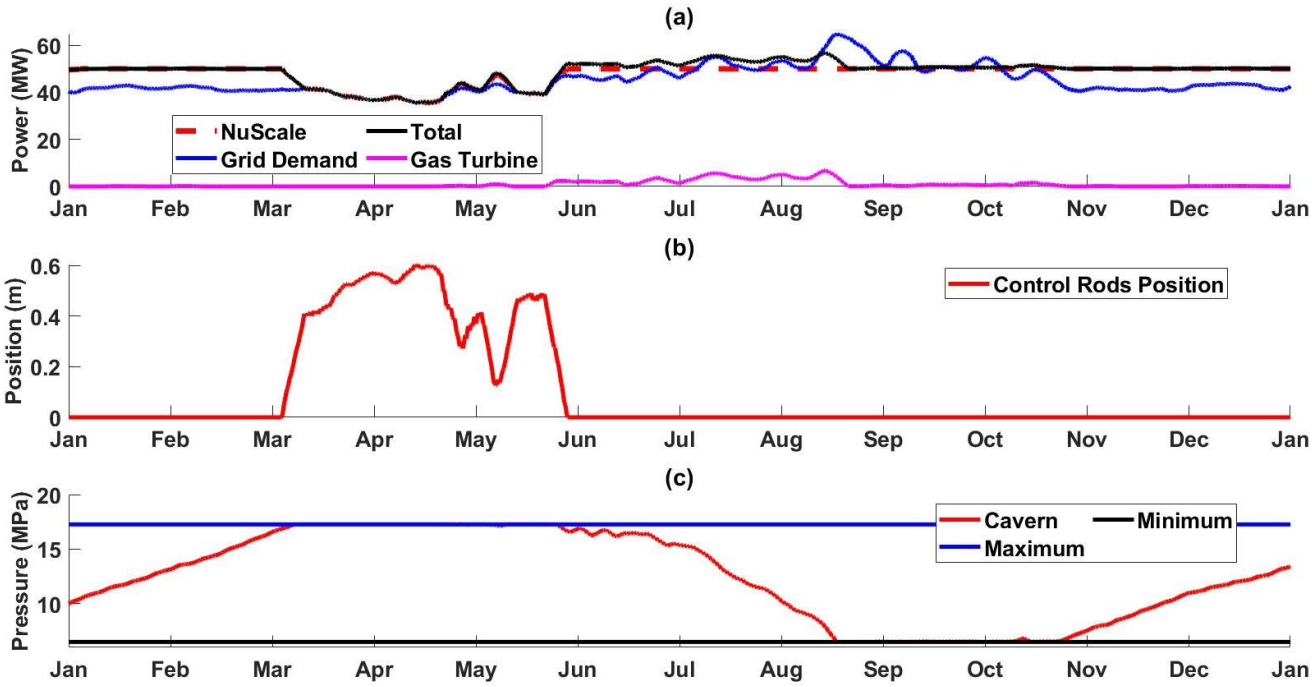

Figure 6. CAISO simulation results: (a) power output of NHES, (b) control rods position of the NuScale plant, and (c) pressure in salt cavern storage.

As shown in Figure 6 (a), 9 out of 12 months in 2020, the nuclear power plant of the NHES does not need to regulate its power output through changing its control rods position. This is due to the addition of the hydrogen generation and storage as well as the gas turbine cycle. This allows the nuclear power to run at base load even when demand is low, storing energy in the form of chemical energy of hydrogen inside the underground salt cavern. When demand is higher than the nominal capacity of the steam Rankine cycle, the stored energy can be used in the form of the gas turbine cycle, which takes the hydrogen out of the salt cavern and generate electricity. As a result, 89.71% of the year, the proposed NHES is able to meet the demand from the grid without the need from outside sources of electricity. This can be seen in Figure 6 (a), where demand is presented in blue line, the total amount of electricity generated in black line, the NuScale power output in dashed red line and the gas turbine cycle power output is in pink line. In total, the NHES produced 419 GWh in the year 2020, met 97.69% of the demand, and had a nuclear capacity factor of 95.85%.

As shown in Figure 6 (b), from March to June, the NuScale plant has to ramp down to not overwhelm the grid system. This is due to the low demand from January to March, which leads to the increase of hydrogen inside the salt cavern. By March, the salt cavern is full, as shown in Figure 6 (c). The low demand from March to June continues to keep the salt cavern at full capacity, which makes the NuScale plant to continue operating at flexible operation. In total, the NHES in the CAISO case has 135 ramping cycles, all are from March to June. The average nuclear power output is 47.88 MW, with a standard deviation of 2.156 MW. In total, the NuScale plant has to ramp up and down 20.14% of the year.

By June, the peak demand increased, and the hydrogen was taken out of the salt cavern to be run as fuel for the gas turbine cycle to meet the increase in demand. As seen in Figure 6 (c), by middle of August, the salt cavern was emptied. Yet the peak demand continues to rise throughout August and September, peaking in mid-August. From mid-August to mid-September, the NHES was not capable of meeting the demand of the grid, and additional electricity has to be bought from outside sources. In the year 2020, 10.29% of the year, the demand was not met, as can be seen in Figure 6 (a).

4.2 ERCOT Simulation Results

The simulation results for ERCOT with 7-day rolling average are presented in Figure 7 (a)-(c). The results for ERCOT are very similar to the results for CAISO, with a few minor differences. As shown in Figure 7 (a), the NuScale nuclear plant is able to run at baseload operations for 9 out of 12 months, almost the same amount of time like the CAISO case. In total, the NuScale plant has to ramp up and down 20.27% of the year, compared to 20.14% of the year in the CAISO case. The NHES produced 421 GWh of electricity, higher than the CAISO case.

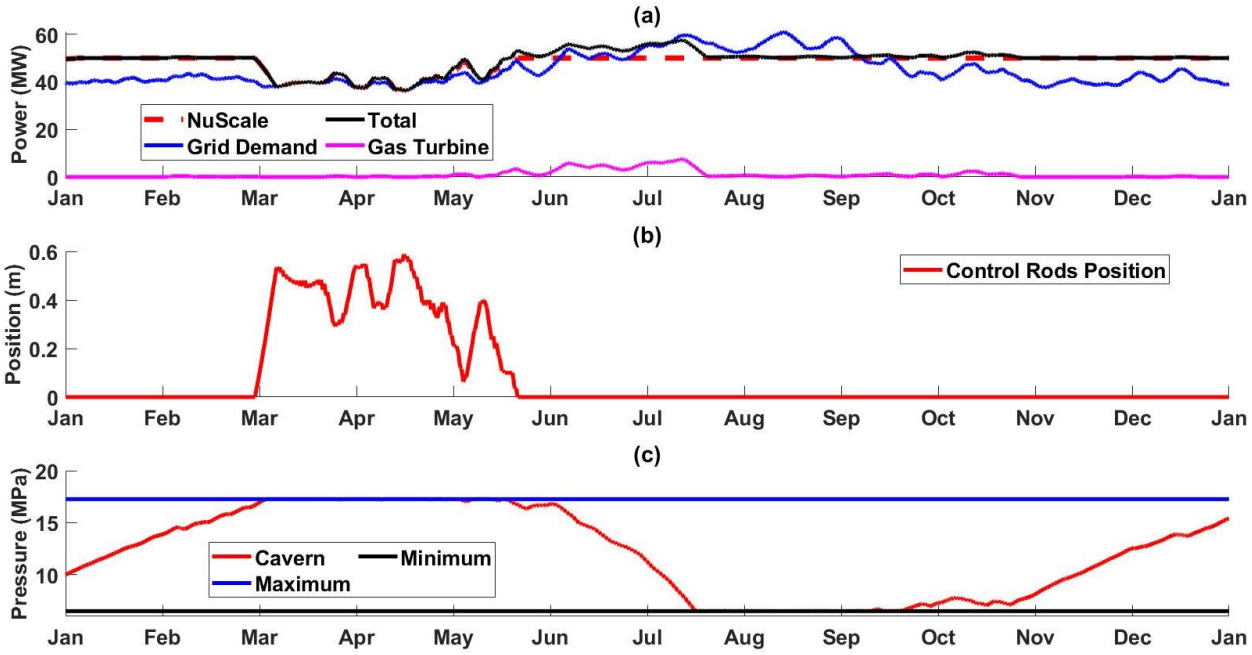

Figure 7. ERCOT simulation results: (a) power output of NHES, (b) control rods position of the NuScale plant, and (c) pressure in salt cavern storage.

However, in the ERCOT case, the NHES is only able to meet the grid demand for 83.89 % of the year, as can be seen in Figure 7 (a). This is because in Texas, the high grid demand peaks are more spread out, with a 7-day rolling average demand rises above the nominal capacity of the NuScale plant starting in early June, and lasting through early September. For California, the 7-day rolling average peak demand only rises above the nominal capacity of the NuScale plant in early July, and ends in early September. This is shown in Figure 8. As a result, the total amount of demand met is slightly slower than that in CAISO: 97.14% to 97.69%.

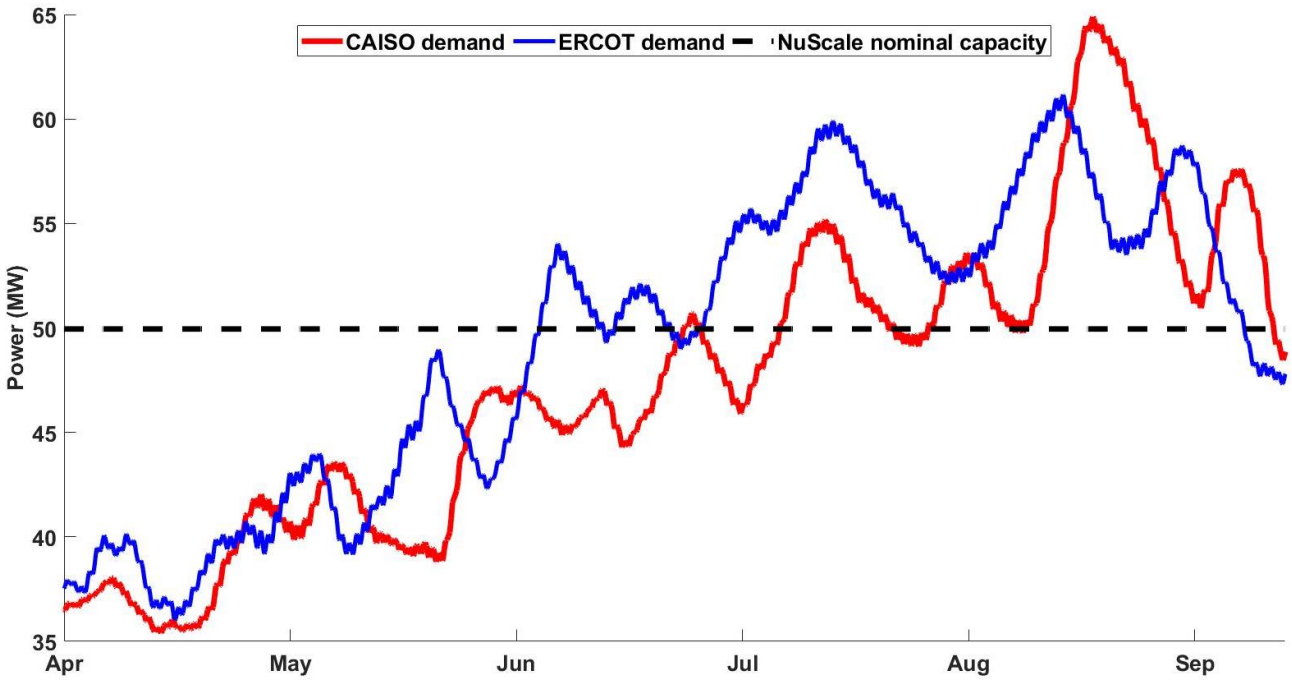

Figure 8. Grid demand comparison between CAISO and ERCOT from April to September 2020

Even though the demand met was less than that in the CAISO case, and the amount of time needed to ramp up and down is relatively the same, ERCOT has significantly fewer ramping cycles than CAISO. In 2020, the NHES only has 82 ramping cycles compared to 135 ramping cycles in CAISO. This can be attributed to two reasons: the grid demand in California can be highly oscillating, where there can be 2 different peak demands in a day. Whereas in Texas, the peak demand is less oscillating. This can be seen in Figure 9. In Figure 9, the grid demand for both CAISO and ERCTO from March to April is shown. The grid demand of CAISO is shown in red, and the demand of ERCOT is shown in blue. As can be seen in Figure 9, the demand in CAISO is a lot more oscillating than ERCOT, with 62 demand peaks in the CAISO case, and only 40 demand peaks in the ERCOT case.

Another reason for this difference is that the demand in ERCOT rises earlier than CAISO, as can be seen in Figure 8. From April to July, the 7-day rolling average of ERCOT grid demand is higher than CAISO grid demand. This means that the ERCOT gas turbine cycle is used more frequently and at higher capacity than the CAISO gas turbine cycle from April to June. This means that the salt cavern is less full in ERCOT than CAISO from April to June, which enables the ERCOT NuScale plant to run at baseload more often than the CAISO NuScale plant from April to June. Less frequent ramping means more nuclear capacity factor, higher average nuclear power output, and lower nuclear power output standard deviation: 96.27% compared to 95.85% nuclear capacity factor; 48.09 MW compared to 47.88 MW average nuclear output; and 1.951 MW compared to 2.156 MW nuclear output standard deviation.

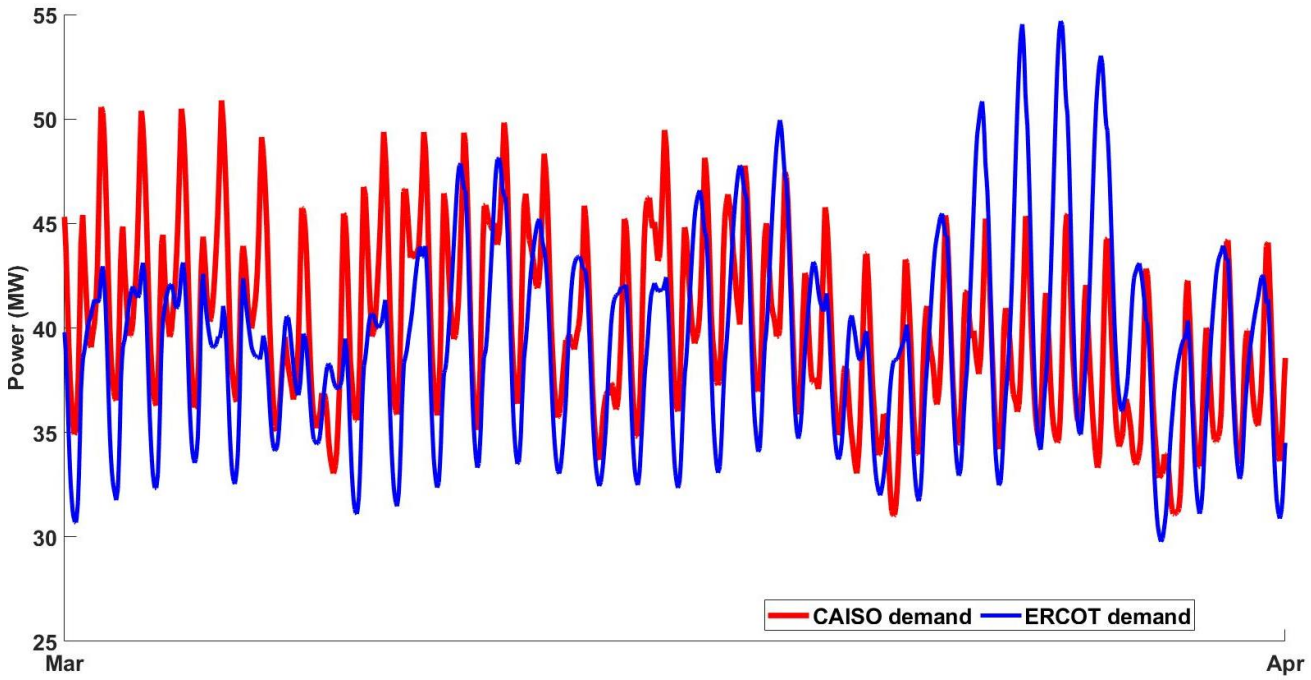

Figure 9. Demand comparison between CAISO and ERCOT

4.3 ISO NEW ENGLAND Simulation Results

The results of the year-long simulation of the NHES study, with 7-day rolling average are shown in Figure 10 (a)-(c). According to Figure 10 (a), the NHES is capable of flexibly providing the required electricity to the grid demand 93% of the year, which is significantly higher than both ERCOT and CAISO, which stands at 89.71% and 83.89% respectively.

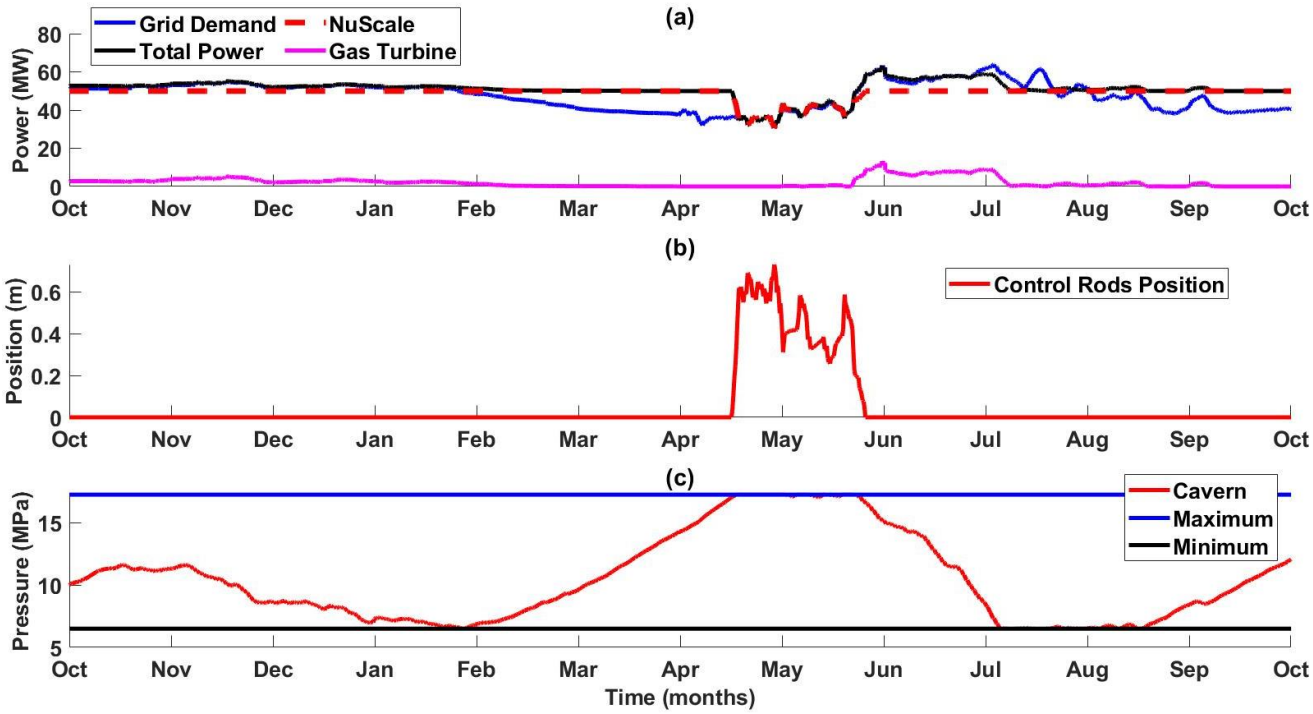

Figure 10. ISO NEW ENGLAND simulation results

Figure 10 (b) shows the stability of the nuclear power plant, only needing to ramp 7.4% of the year, which is once again, remarkably lower than the CAISO and ERCOT cases, which are 20.14% and 20.27% respectively. This is because for ISO NEW ENGLAND, demand is significantly higher at the beginning of the year compared to ERCOT and CAISO, as shown in Figure 11. Figure 11 shows the 7-day rolling average demand of ISO NEW ENGLAND, CAISO and ERCOT. As seen in Figure 11, the demand at the beginning of the year for ISO NEW ENGLAND is significantly higher than that of CAISO and ERCOT, with the ISO NEW ENGLAND demand average of 51.64 MW, compared to 42.18 MW and 40.32 MW for CAISO and ERCOT respectively. This is due to the necessity of heating in New England during the winter, where the temperature gets significantly colder than CAISO and ERCOT. This results in the need for extra electricity generated by the gas turbine cycle in the ISO NEW ENGLAND case. This means that the underground salt cavern in ISO NEW ENGLAND doesn't get full in March, but in mid-April. The ISO NEW ENGLAND demand also picks up before June, reducing the amount of time the underground salt cavern is full.

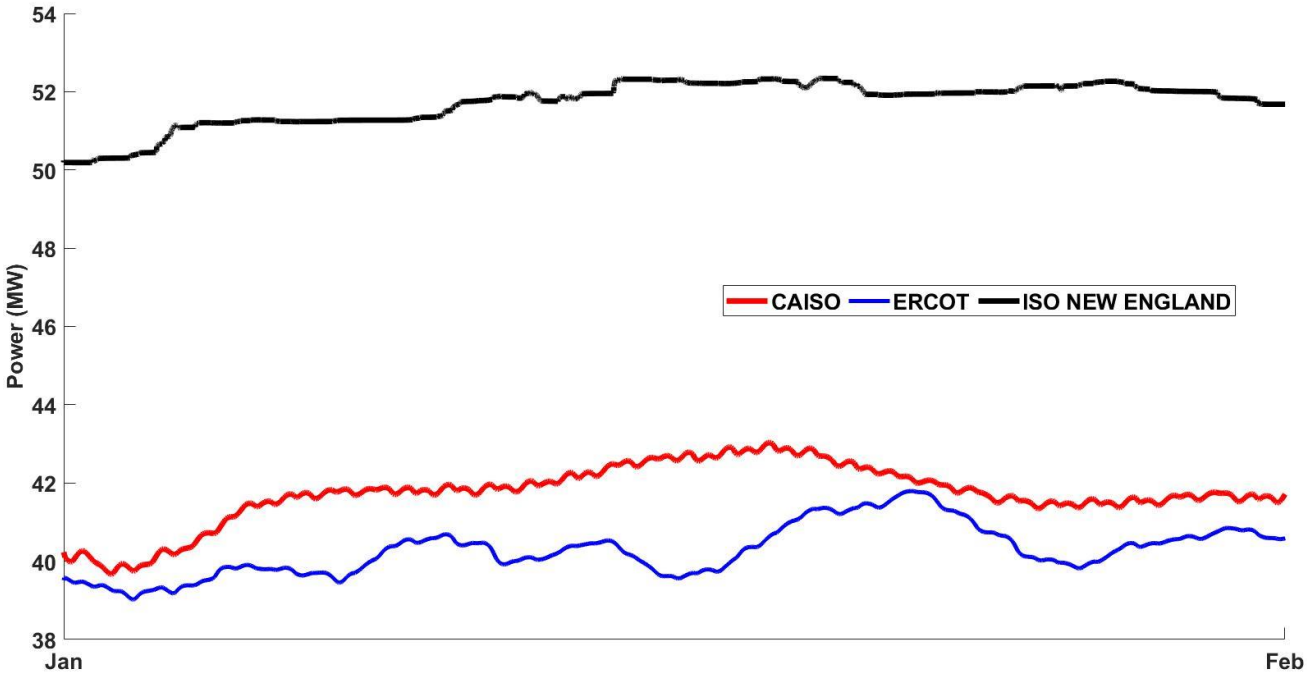

Figure 11. 7-day rolling average of grid demand for ISO NEW ENGLAND, CAISO, and ERCOT

Table 10 shows the results for the different criteria chosen for comparison. ISO NEW ENGLAND has the highest nuclear capacity factor as well as total power produced. ISO NEW ENGLAND meet the most demand percentage wise as well as time wise. This means that ISO NEW ENGLAND NuScale has the least amount of time ramping up and down, as well as the least number of ramping cycles. This means in a technical perspective, ISO NEW ENGLAND is the most beneficial location for the proposed NHES in the three locations.

Table 7

Summary table of comparison between the three ISO's: ISO NEW ENGLAND, CAISO, and ERCOT.

Parameters	ISO NE	CAISO	ERCOT
Nuclear capacity factor	98.3%	95.85 %	96.27 %
Total power produced (MWh)	443×10^3	419×10^3	421×10^3
Percentage of total demand met	98.39 %	97.69 %	97.14 %
Percentage of time when demand is met	93 %	89.71 %	83.89 %
Total number of cycles	39	135	82

Standard deviation of nuclear power output	0.808 MW	2.156 MW	1.951 MW
Percentage of time ramping up and down	7.4%	20.14%	20.27 %

5. Conclusion

Ultimately, this integrated model makes it possible to analyze different grid demand trends to find which would be best suited to incorporate a Nuclear Hybrid Energy System. Based on the performance metrics for each of the grid demand datasets analyzed so far, this hybrid energy system would be best suited for the ISO New England grid. This grid had the least amount of nuclear ramping cycles (39 in total) while also maintaining the highest percent of total demand met (98.39%). Additionally, it had the highest percentage of time where grid demand was met (93%) and spent significantly less time ramping up and down than the other two data sets (7.4%). The simulation performed better in New England because the New England grid maintained a more consistent energy demand throughout the year, which can be seen mostly clearly in Figure 11 where demand in January and February was much higher than the same months in California and Texas.

For future work it is recommended to incorporate an economic analysis into the simulation to see which location would be most profitable for the Hybrid energy system. Additionally, research needs to be done to find where available salt caverns are located to determine where the NHES is feasible.

References

[1] R. Pinsky, P. Sabharwall, J. Hartvigsen and J. O'Brien, "Comparative review of hydrogen production technologies for nuclear hybrid energy systems," *Progress in Nuclear Energy*, 2020.

[2] S. Moataz and K. Powell, "Using Real-Time Electricity Prices to Leverage Electrical Energy Storage and Flexible Loads in a Smart Grid Environment Utilizing Machine Learning Techniques," *Processes*, vol. 7, 2019.

[3] S. Moataz, K. Mohammadi and K. Powell, "Techno-economic analysis of the impact of dynamic electricity prices on solar penetration in a smart grid environment with distributed energy storage," *Applied Energy*, vol. 282, 2021.

[4] M. R. Abdussami, M. I. Adham and H. A. Gabbar, "Modeling and performance analysis of nuclear-renewable micro hybrid energy system based on different coupling methods," *Energy Reports*, vol. 6, pp. 189-206, 2020.

[5] J. F. Tuttle and K. M. Powell, "Analysis of a thermal generator's participation in the Western Energy Imbalance Market and the resulting effects on overall performance and emissions," *The Electricity Journal*, vol. 32, no. 5, pp. 38-46, 2019.

[6] A. Epiney, C. Rabiti, P. Talbot and A. Alfonsi, "Economic analysis of a nuclear hybrid energy system in a stochastic environment including wind turbines in an electricity grid," *Applied Energy*, 2020.

[7] S. Moataz, K. Mohammadi and K. Powell, "Solving the duck curve in a smart grid environment using a non-cooperative game theory and dynamic pricing profiles," *Energy Conversion and Management*, vol. 220, 2020.

[8] J. S. Kim, K. M. Powell and T. F. Edgar, "Nonlinear Model Predictive Control for a Heavy-Duty as Turbine Power Plant," in *American control conference*, Washington D.C., 2013.

[9] B. S. Palmintier and M. D. Webster, "Impact of operational flexibility on generation planning with renewable and carbon targets," *IEEE Trans Sustain Energy*, 2016.

[10] F. J. Sisternes, J. D. Jenkins and A. Botterud, "The value of energy storage in decarbonizing the electricity sector," *Applied Energy*, 2016.

[11] S. Suman, "Hybrid nuclear-renewable energy systems: A review," *Journal of Cleaner Production*, 2018.

[12] J. D. Jenkins, Z. Zhou, R. Ponciroli, R. B. Vilim, F. Ganda, F. de Sisternes and A. Botterud, "The benefits of nuclear flexibility in power system operations with renewable energy," *Applied Energy*, 2018.

[13] C. Forsberg, "Meeting Low-Carbon Industrial Heat Demand with High-Temperature Reactors Using Co-Generation and Heat Storage, Vol. 120," *Transactions of the American Nuclear Society,* 2019.

[14] J. H. Keppler and M. Cometto, "Nuclear energy and renewables: system effects in low-carbon electricity systems.," *Nuclear Energy Agency,* 2012.

[15] H. Ludwig, T. Salnikova, A. Stockman and U. Waas, "Load cycling capabilities of German Nuclear Power Plants (NPP).," *Int J Nucl Power,* 2010.

[16] D. Machalek and K. Powell, "Automated electrical demand peak leveling in a manufacturing facility with short term energy storage for smart grid participation," *Journal of Manufacturing Systems,* vol. 52, pp. 100-109, 2019.

[17] D. Machalek, A. Young, L. Blackburn, P. Rogers and K. M. Powell, "Mine operations as a smart grid resource: Leveraging excess process storage capacity to better enable renewable energy sources," *Minerals Engineering,* vol. 145, p. 106103, 2020.

[18] P. Brimley, D. Machalek and K. Powell, "Smart Scheduling of a Batch Manufacturer's Operations by Utilization of a Genetic Algorithm to Minimize Electrical Demand," *Smart and Sustainable Manufacturing Systems,* vol. 3, no. 2, p. 20190018, 2019.

[19] P. Nikolaidis and A. Poullikkas, "A comparative overview of hydrogen production processes," *Renew. Sustain. Energy Rev,* 2017.

[20] M. El-Shafie, S. Kambara and Y. Hayakawa, "Hydrogen production technologies overview," *J. Power Energy Eng,* 2019.

[21] International Energy Agency, "The Future of Hydrogen," Paris, 2019.

[22] B. Sedaee, M. Mohammadi, L. Esfahanizadeh and Y. Fath, "Comprehensive modeling and developing a software for salt cavern underground gas storage," *Journal of Energy Storage,* 2019.

[23] D. G. Caglayan, N. Weber, H. Heinrichs, J. Linßen, M. Robinius, P. A. Kukla and D. Stolten, "Technical Potential of Salt Caverns for Hydrogen Storage in Europe," *International Journal of Hydrogen Energy,* 2020.

[24] H. Landinger, and F. Crotogino, "The role of large-scale hydrogen storage for future renewable energy utilisation," *Second International Renewable Energy Storage Conference,* 2007.

[25] OFFICE of FOSSIL ENERGY, U.S. Department of Energy, "Strategic Petroleum Reserve," 2021.

[26] Y. Wang, J. Kowal, M. Leuthold and D. U. Sauer, "“Storage System of Renewable Energy Generated Hydrogen for Chemical Industry," *Energy Procedia,* pp. 657-667, 2012.

[27] D. T. Ingersoll, Z. J. Houghton, R. Bromm, and C. Desportes, "NuScale small modular reactor for Co-generation of electricity and water," *Desalination,* 2014.

[28] B.-c. Zhao, M.-s. Cheng, C. Liu and Z.-m. Dai, "Conceptual design and preliminary performance analysis of a hybrid nuclear-solar power system with molten-salt packed-bed thermal energy storage for on-demand power supply," *Energy Conversion and Management*, 2018.

[29] R. S. El-Emam, H. Ozcan and C. Zamfirescu, "Updates on promising thermochemical cycles for clean hydrogen production using nuclear energy," *Journal of Cleaner Production*, 2020.

[30] S. Şahin and H. M. Şahin, "Generation-IV reactors and nuclear hydrogen production," *International Journal of Hydrogen Energy*, 2021.

[31] J. E. O'Brien, M. G. McKellar, E. A. Harvego and C. M. Stoots, "High-temperature electrolysis for large-scale hydrogen and syngas production from nuclear energy – summary of system simulation and economic analyses," *Int J Hydrogen Energy*, 2010.

[32] NRC, "Design Certification Application - NuScale," December 2020. [Online]. Available: https://www.nrc.gov/reactors/new-reactors/smr/nuscale.html.

[33] D. S. Falcao and A. Pinto, "A review on PEM electrolyzer modelling: Guidelines for beginners," *Journal of Cleaner Production*, 2020.

[34] Modern Power Systems, "Gas turbines in the US are being prepped for a hydrogen-fuelled future," *NS Energy*, 6 Jan 2021.

[35] MathWorks Inc., "MATLAB and Statistics Toobox Release 2020b," MathWorks Inc., Natick, MA, USA, 2020.

[36] A. Gabor, C. Fazeska and K. M. Hangos, "Modeling and Identification of a Nuclear Reactor with Temperature Effects and Xenon poisoning," in *IEEE Xplore*, 2009.

[37] K. Frick, "Status Report on the NuScale Module Developed in the Modelica Framework," Idaho National Lab, 2019.

[38] M. Johnson, S. Lucas and P. Tsvetkov, "Modeling of Reactor Kinetics and Dynamics," INL, Idaho Falls, 2010.

[39] A. Sadegh-Noedoost, F. Faghihi, A. Fakhraei and M. Amin-Mozafari, "Investigations of the fresh-core cycle-length and the average fuel depletion analysis of the NuScale core," *Annals of Nuclear Energy*, vol. 136, February 2020.

[40] D. L. Hetrick, Dynamics of Nuclear Reactors, USA: American Nuclear Society, 1993.

[41] F. D'Auria, Thermal-Hydraulics of Water Cooled Nuclear Reactors, Woodhead Publishing, 2017.

[42] F. Marangio and M. G. L. Santarelli, "Theoretical model and experimental analysis of a high pressure PEM water electrolyser for hydrogen production," *International Journal of Hydrogen Energy*, pp. 1143-1158, 2009.

[43] T. Yigit and O. F. Selamet, "Mathematical modeling and dynamic Simulink simulation of high-pressure PEM electrolyzer system," *International Journal of Hydrogen Energy,* pp. 13901-13914, 2016.

[44] M. M. Tomadakis and S. V. Sotirchos, "Ordinary and transition regime diffusion in random fiber structures," *AICHE Journal,* 1993.

[45] M. Santarelli, "idrogeno e celle a combustibile".

[46] M. G. L. Santarelli, M. F. Torchio and P. Cochis, "Parameters estimation of a PEM fuel cell polarization curve and analysis of their behavior with temperature," *Journal of Power Sources,* pp. 824-835, 2006.

[47] J. C. Amphlett, R. M. Baumert, R. F. Mann, B. A. Peppley, P. R. Roberge and T. J. Harris;, "Performance modelling of the ballard mark iv solid polymer electrolyte fuel cell," *Journal of The Electrochemical Society,* vol. 142, 1995.

[48] J. H. Nam and M. Kaviany, "Effective diffusivity and water-saturation distribution in single- and two-layer PEMFC diffusion medium," *International Journal of Heat and Mass Transfer,* vol. 46, no. 24, pp. 4595-4611, 2003.

[49] Rajeshwar, M. Krishnan and L. Robert, Solar hydrogen generation, toward a renewable energy future, Springer, 2008.

[50] F. Incropera, D. DeWitt, T. Bergman and A. Lavine, Fundamentals of Heat and Mass Transfer, John Wiley & Sons, 2006.

[51] E. W. Lemmon, M. L. Huber and J. W. Leachman, "Revised Standardized Equation for Hydrogen Gas Densities for Fuel Consumption Applications," *Journal of Research of the National Institute of Standards and Technology,* vol. 113, no. 6, p. 341–350, 1 December 2008.

[52] A. Witkowski, A. Rusin, M. Majkut and K. Stolecka, "Comprehensive analysis of hydrogen compression and pipeline transportation from thermodynamics and safety aspects," *Energy,* vol. 141, pp. 2508-2518, 15 December 2017.

[53] HyUnder, "Assessment of the potential, the actors and relevant business cases for large scale and seasonal storage of renewable electricity by hydrogen underground storage in Europe," 2014.

[54] M. Henning, D. Machalek and K. Powell, "Integrating a Microturbine into a Discrete Manufacturing Process with Combined Heat and Power Using Smart Scheduling and Automation," *Computer Aided Chemical Engineering,* vol. 47, pp. 293-298, 2019.

[55] K. Ellingwood, K. Mohammadi and K. Powell, "A novel means to flexibly operate a hybrid concentrated solar power plant and improve operation during non-ideal direct normal irradiation conditions," *Energy Conversion and Management,* 2020.

[56] P. Gabrielli, A. Poluzzi, G. J. Kramer, C. Spiers, M. Mazzotti and M. Gazzani, "Seasonal energy storage for zero-emissions multi-energy systems via underground hydrogen storage," *Renewable and Sustainable Energy Reviews,* vol. 121, 2020.

[57] Mitsubishi Power, "MHPS Successfully Tests Large-scale High-efficiency Gas Turbine Fueled by 30% Hydrogen Mix -- Will Contribute to Reducing CO2 Emissions during Power Generation --," *Mitsubishi Power,* 19 Jan 2018.

[58] CAISO, "Historical EMS Hourly Load Data Available," 2021. [Online]. Available: https://www.caiso.com/Documents/HistoricalEMSHourlyLoadDataAvailable.html.

[59] ERCOT, "Hourly Load Data Archives," 2021. [Online]. Available: http://www.ercot.com/gridinfo/load/load_hist/.

[60] ISO New England, "Energy, Load, and Demand Reports," 2021.